Cellular heterogeneity in pressure and growth emerges from tissue topology and geometry

Yuchen Long[1,*], Ibrahim Cheddadi[2,3], Vincent Mirabet[1], Mathilde Dumond[1,4], Christophe Godin[1,2], Arezki Boudaoud[1,*].

1. Laboratoire Reproduction et Développement des Plantes, Univ Lyon, ENS de Lyon, UCB Lyon 1, CNRS, INRA, INRIA, F-69342, Lyon, France.

2. INRIA/CIRAD/INRA Project-team Virtual Plants, France.

3. Current address: Laboratoire TIMC-IMAG/DyCTiM, Université Grenoble Alpes, CNRS, UMR 5525, 38706 La Tronche, France.

4. Current address: Department of Biosystems Science and Engineering, ETH Zurich, Mattenstrasse 26, 4058, Basel, Switzerland.

*. Correspondence and requests for materials should be addressed to yuchen.long@ens-lyon.fr or arezki.boudaoud@ens-lyon.fr

The authors declare no competing financial interests.

Summary

Cell-to-cell heterogeneity is observed in many biological phenomena like gene expression, signalling, cell size regulation and growth[1–8]. Notably, heterogeneity in cell size and growth rate prevails in many systems and impacts tissue patterning and macroscopic growth robustness[1,2]. From physical perspective, cell volume change is driven by osmosis[9–11] and the subsequent intracellular hydrostatic pressure, which sustains cellular osmotic potential and is confined by peripheral constraints (plasma membrane, cytoskeletal cortex, extracellular matrix or cell wall) in plant[12], animal[13], tumorous[14] and microbial cells[15]. Despite numerous studies in unicellular systems[15,16], the spatial variation of hydrostatic pressure in multicellular tissues, and its relation with cell-to-cell growth variability, remain elusive. Here, using atomic force microscopy, we demonstrate that hydrostatic pressure is highly heterogeneous between adjacent cells in the epidermis of Arabidopsis shoot apical meristem, and it unexpectedly

correlates either positively or negatively with cellular growth rate depending on growth conditions. Combining experimental arguments and physical modelling of cell wall mechanics and osmosis within multicellular tissues, we show that heterogeneities in pressure and growth are not random, and they spontaneously emerge from cell size and tissue topology. Together, we propose that cellular pressure build-up, a physical phenomenon, and growth rate, a biological property, are innately heterogeneous and modulate cell size homeostasis in any compact tissue with inhomogeneous topology.

One sentence summary

Tissue geometry and topology prescribe heterogeneity in hydrostatic pressure and growth.

Key words

Cellular heterogeneity, hydrostatic pressure, tissue topology, growth mechanics, atomic force microscopy, biophysical modelling.

Main text

Growth is driven by osmosis and constrained by cell envelop. Cells with rigid cell walls – like in plants, bacteria and fungi – can sustain high osmotic potential by accumulating hydrostatic pressure, alias turgor pressure, greater than atmospheric pressure (Extended Data Fig. 1)[12]. Animal cells also accumulate hydrostatic pressure, especially when compacted or contracting[13,14]. In plants, turgor pressure is believed to positively correlate with growth rate, as depicted in the Lockhart-Ortega equation (Extended Data Fig. 1)[17]. However, observations suggest that growth rate and pressure level are not always associated[16], challenging the link between growth regulation and cellular pressure build-up.

Recent advances in atomic force microscopy (AFM) enabled non-invasive turgor pressure measurement utilizing indentation force-displacement and surface topography in living plant cells (Fig. 1A)[18]. We took advantage of these advances and assessed the relation between cell-specific turgor pressure and growth in the epidermis of the *Arabidopsis thaliana* shoot apical meristem (SAM), a system featuring substantial growth heterogeneity[1]. We included

untreated wild-type SAM and a conceptually simpler model of chemically treated SAM that resembles a "foam of cells" (co-treated with naphthylphthalamic acid (NPA), a polar auxin transport inhibitor that induces pin-formed SAM, and oryzalin, a microtubule-depolymerizing drug that blocks cell division but permits continuous, isotropic growth; hereafter referred to as "oryzalin-treated SAM",)[19].

Cell walls are often curved in oryzalin-treated SAM, suggesting that neighbouring cells have different turgor pressure[19]. Cell-specific AFM measurements on nine SAMs revealed that turgor pressure is markedly heterogeneous in oryzalin-treated SAM epidermis (Fig. 1E). Each SAM had a different average turgor pressure (Extended Data Fig. 2), consistent with previous report[20]. We subtracted this difference by normalizing cellular pressure to the average pressure per SAM, and found that turgor pressure anticorrelates with the number of epidermal cell-neighbours: cells with fewer neighbours have higher turgor pressure, with 1.4-fold difference between four and eight-neighboured cells (n = 202 cells, Pearson correlation coefficient R = -0.34, $p < 10^{-6}$) (Fig. 1F), consistent with previous prediction[19]. In untreated SAMs, we also detected similar turgor–neighbour-number anticorrelation (5 SAMs, n = 326 cells, R = -0.16, p = 0.004) (Fig. 1G-J, Extended Data Fig. 3), confirming that non-random turgor pressure heterogeneity establish robustly in tissues with static topology (no neighbour number change) or dynamic topology (neighbour number changes due to division).

Earlier works[19,21] treated intracellular pressure as an input or required differential osmotic pressure. We explored the topological association of turgor pressure variability by constructing a 2D vertex model, with topological distribution similar to SAM (Extended Data Fig. 4), attributing turgor build-up and in-tissue water flow to osmosis and wall mechanics (Cheddadi et al. unpublished) (Fig. 2A). The model expands the Lockhart-Ortega equation of visco-elasto-plastic growth of single cell (Extended Data Fig. 1)[17] to cell walls in a multicellular tissue with more realistic 2D polygonal geometry. Cell wall growth is akin to visco-plastic flow (irreversible deformation) and occurs when elastic strain (reversible deformation) induced by turgor pressure is greater than a threshold (Fig. 2A). Water influx follows the cross-membrane water potential difference, and turgor-driven intercellular water redistribution is allowed via plant plasmodesmata[22], animal gap junctions or cytoplasmic

bridges[23,24]. We did not prescribe turgor pressure, instead letting it emerge from local mechanical and hydraulic interplays. Surprisingly, with homogenous cellular parameters, we could recover the turgor–neighbour-number anticorrelation in our model, without or with cell divisions to mimic oryzalin-treated or untreated SAM (no division 5 simulations, n = 1219 cells, R = -0.87, $p < 10^{-100}$; dividing 8 simulations, n = 3240 cells, R = -0.58, $p < 10^{-100}$) (Fig. 2B-G). This implies that local hydrostatic pressure heterogeneity does not require differential cellular osmotic pressure[19], and predicts a topological origin of pressure variability, similar to liquid foams[25].

In SAM surface, cell neighbour number and size are coupled (Extended Data Fig. 4). Consistently, cell-specific turgor pressure anticorrelates with normalized cell area (Extended Data Fig. 4). We modified the initial state of our simulation to have four-neighboured cells bigger than eight-neighboured cells, and found that higher turgor pressure accumulated in four-neighboured cells, not in the smaller cells (Extended Data Fig. 4), confirming that turgor pressure heterogeneity emerges from tissue topology rather than cell size differences. This can be explained by local topology, which determines cell wall angles and the subsequent tension distribution at each three-cell junction (Fig. 2H-K): in our model with wall rheology and hydraulic limitations, elastic strain (relative deformation) and stress (tension) are capped slightly above the growth-threshold, and are almost homogeneous in the tissue. Therefore, the sum of wall tension at each three-cell junction (vertex) depends only on the angles between walls. The vertex between three hexagonal cells with 120 ° internal angles has a sum of tension at zero (Fig. 2H, I). Fewer-neighboured cells have sharper internal angles, so the sum of tension at vertex is greater towards the cell interior, creating additional inward compression and prompting higher pressure build-up at equilibrium (Fig. 2J, K). Since topology is highly conserved in many biological systems[26], we propose that hydrostatic pressure heterogeneity is an innate characteristic of any compact tissue with polygonal cells[27], which adjusts itself to reconcile local mechanical and hydraulic conditions.

Next, we monitored areal growth rate of SAM epidermal cells by time-lapse confocal microscopy. Growth rate in untreated SAMs anticorrelates with neighbour number (11 SAMs, n = 2013 cells, R = -0.13, $p < 10^{-8}$; Fig. 3E) and cell size (Fig. 3F; R = -0.28, $p < 10^{-36}$),

supporting previous reports that smaller cells in SAM grow faster[28,29], and suggests that higher turgor pressure in fewer-neighboured cells associates with faster growth. Unexpectedly, in oryzalin-treated SAMs, the fewer-neighboured and small cells grew slower (14 SAMs, n = 1160 cells; Fig. 3K, neighbour number R = 0.14, $p < 10^{-5}$; Fig. 3L, cell size R = 0.22, $p = 10^{-14}$). This suggests that higher turgor pressure associates with either faster or slower growth depending on conditions (Extended Data Fig. 4). Although seemingly a small shift, this negative-to-positive slope change of local growth heterogeneity captures a strong qualitative inversion of growth behaviour (Fig. 3D, J), where relative cell size increases exponentially in opposite fashions (Extended Data Fig. 5).

We explored growth variability with our model: Non-random growth heterogeneity emerged from homogenous parametric inputs, with the smaller, fewer-neighboured cells growing faster (8 simulations, n = 3240 cells; G vs N, R = -0.05, p = 0.002, Fig. 4B; G vs A, R = -0.82, $p < 10^{-100}$) that recapitulates untreated SAM (Fig. 3A-F). We attempted to simulate oryzalin-treated SAM by blocking cell division, but found it not sufficient to invert the topology-growth trend (Fig. 4D-F), indicating that additional parameter changes are needed to recapitulate oryzalin-treated growth heterogeneity.

Our model predicts two antagonistic phenomena that impact growth: growth rate depends on water access across cell surface, so smaller cells benefit from higher surface-versus-volume ratio for relatively more water influx and volume increase; meanwhile, the often-smaller fewer-neighboured cells are under extra mechanical compression due to tissue topology (Fig. 2K) and would grow slower. Since the often-smaller fewer-neighboured cells grow faster in untreated meristems, the model suggests that flux limitation is predominant in this condition, while oryzalin treatment elevates the relative importance of the mechanical limitation. We explored the parameter space of the model, and found that raising strain threshold or decreasing osmotic pressure can elevate the predominance of mechanical constraint (Fig. 4G-L), effectively switching the foam-like system from cell-size-and-flux-controlling to topology-and-mechanic-controlling (Extended Data Fig. 6).

Interestingly, growth rate correlates better with cell size in simulations representing untreated

SAM growth trends (Fig. 4A-F) or with neighbour number in oryzalin-like models (Fig. 4G-L). We tested this experimentally, focusing on the slope of growth rate against neighbour number or cell size, and found that level of growth heterogeneity in individual SAMs correlates with average SAM growth rate (Extended Data Fig. 6): topology-associated growth heterogeneity is stronger in fast-growing oryzalin-treated SAMs (n = 14 SAMs, R = 0.63, p = 0.02 < 0.05), while size-associated growth heterogeneity is stronger in slow-growing untreated SAMs (n = 11 SAMs, R = 0.68, p = 0.02 < 0.05) (Extended Data Fig. 6). No significant correlation of size-associated growth heterogeneity was found in oryzalin-treated SAMs (R = 0.14, p = 0.53 > 0.05), neither topology-associated correlation in untreated SAMs (R = 0.56, p = 0.07 > 0.05). This indicates that growth heterogeneity is more sensitive to size-related properties in untreated SAMs, or to topology-related properties in oryzalin-treated SAMs, as predicted by the model and unlike liquid foams where topology always dominates. Furthermore, it shows that growth heterogeneity scales with global growth speed, where faster growth enhances the cell size diverging effect of oryzalin treatment, and reduces the cell size homogenizing tendency in untreated scenario (Extended Data Fig. 6), suggesting that faster tissue growth favours enhanced cell size variability.

Together, we demonstrate that cellular hydrostatic pressure is innately heterogeneous in Arabidopsis SAM epidermis, however it is not a proxy of local growth rate variability, as previously believed. Instead, turgor pressure and growth rate are combinatorial outputs of local mechanics and hydraulics. Each of these parameters can be controlled by genetic and biochemical inputs, and small changes in these biological inputs can enable drastic shifts of cell size distribution (Extended Data Fig. 6), unlike liquid foams in which cell size distribution always enlarge over time. For example, a growth variability switch is observed during sepal development, where smaller and often fewer-neighboured cells grow faster in young sepals then slower in older sepals, effectively switching from homogenizing to amplifying cell size variability[30]. The emergent heterogeneity of local growth and hydrostatic pressure likely underlies morphogenesis in other compact tissues with polygonal cells.

Acknowledgements

We thank L. Beauzamy for AFM training and G. Cerrutti for help in implementing the division algorithm. This work was supported by a fellowship from Institut Universitaire de France and an ERC Starting Grant "PhyMorph" to A.B. (ERC-2012-StG-307387), an EMBO Long-term Fellowship to Y.L. (EMBO ALTF 168-2015), and an Agropolis Foundation grant (MecaFruit3D) to I.C. and C.G.

Author contributions

This study was initiated by A.B. Y.L. and A.B. designed the experiments. Y.L. executed AFM and confocal microscopy, acquired and analysed experimental data. I.C. and C.G. designed physical model. I.C. implemented the model, ran simulations, optimized model parameters and analysed simulation data. V.M and M.D. wrote scripts to facilitate experimental data subtraction and analysis. Y.L. and A.B. wrote the manuscript with inputs from other authors. Y.L., I.C., M.V., M.D., C.G. and A.B. contributed to data interpretation and critical reading of the manuscript.

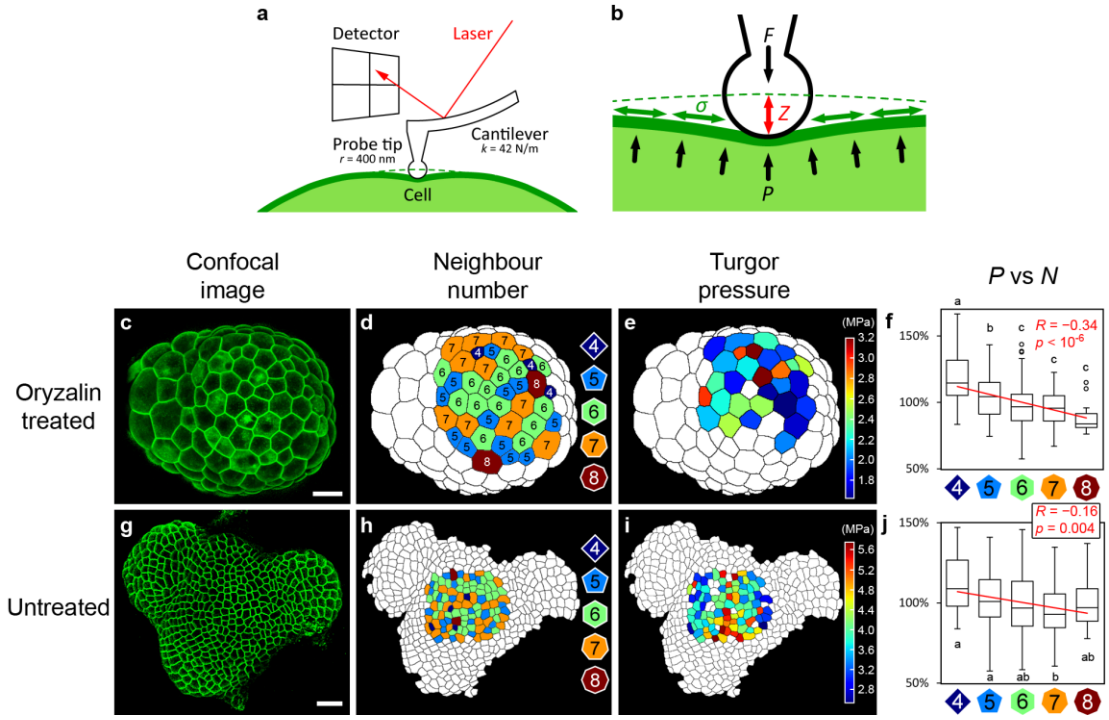

Figure 1. Turgor pressure heterogeneity in SAM is associated with variation of cell topology.

(**a** and **b**) Schematic representation of AFM nanoindentation for turgor pressure measurement. *r*, probe tip radius; *k*, cantilever stiffness; *F*, indentation force; *Z*, indentation depth; *P*, turgor pressure; σ, cell wall tension. (**c** to **j**) Cell-specific turgor pressure in oryzalin-treated (c to f) and untreated SAM (g to j). (c and g) Top-view surface projections of SAM, oryzalin-treated (c) or untreated (g), with plasma membrane GFP signal; scale bars represent 20 μm. (d and h) Cell topology determined on segmented cell contour images, around SAM centre; numbers indicate neighbour number in epidermis. (e and i) AFM-determined cell-specific turgor pressure heat maps. (f and j) Box plots of cellular turgor pressure *P* normalized per SAM against cell topology *N* (f, oryzalin-treated 9 SAMs, $n = 202$ cells; j, untreated 5 SAMs, $n = 326$ cells). Circles are Tukey's outliers; lowercase letters indicate statistically different populations (Student's *t*-test, $p < 0.05$); red lines indicate linear regressions, with Pearson correlation coefficient *R* and corresponding *p*-value.

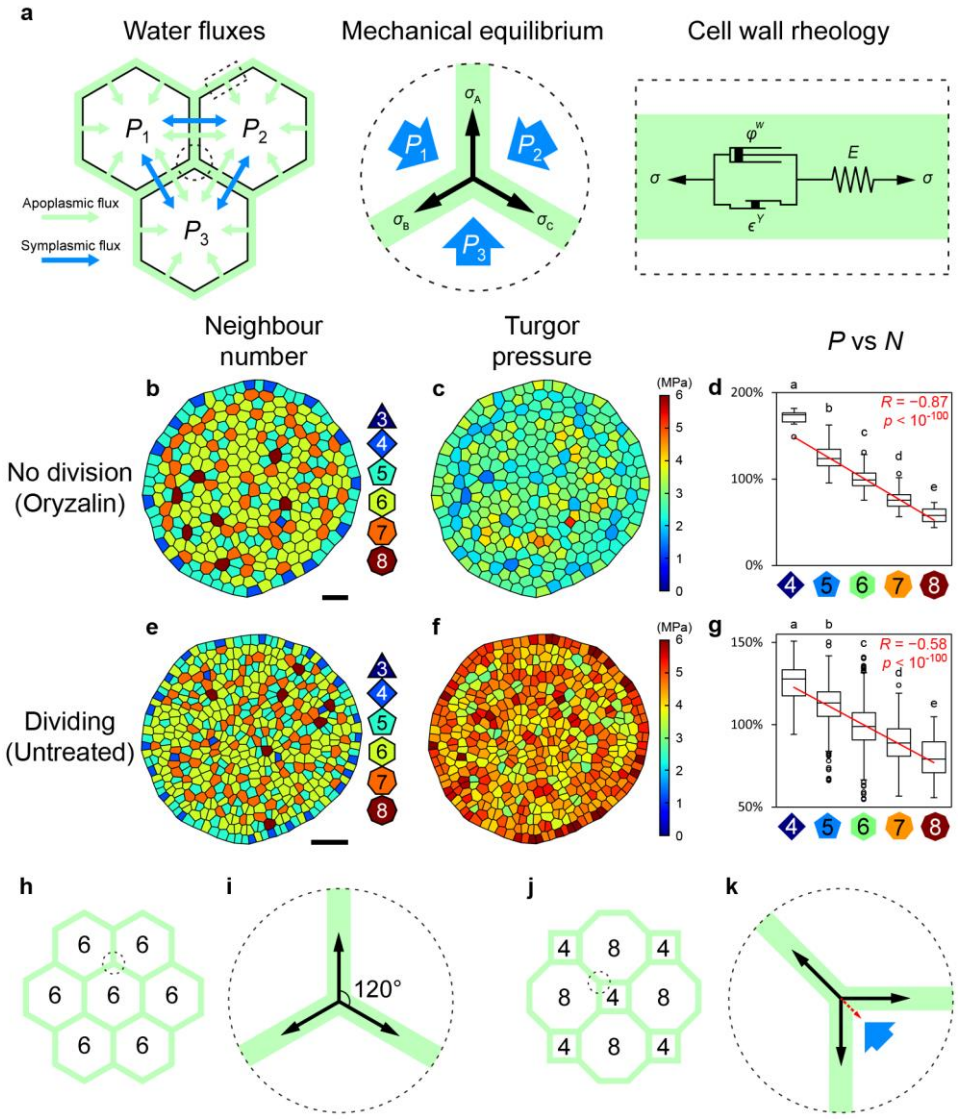

Figure 2.Turgor pressure heterogeneity emerges from cell topology.

(**a**) Schematic representations of model components, including apoplasmic and intercellular water fluxes (left), mechanical equilibrium at three-cell junctions (middle) and the visco-elasto-plastic cell wall rheology. P, cell-specific turgor pressure; σ, cell wall tension; φ^w, wall extensibility; ϵ^Y, wall strain threshold; E, wall Young's modulus. (**b** to **g**) Turgor pressure in non-dividing (oryzalin-treated, b to d) and dividing (untreated) simulations (e to g), scale bars are 5 unit length. (b and e) Cell topology; (c and f) cellular turgor pressure heat maps; (d and g) Box plots of normalized cellular turgor pressure P against cell topology N (d, non-dividing 5 simulations, n = 1219 cells; g, dividing 8 simulations, n = 3240 cells). Cells on the mesh edge were not analysed due to border effect. Circles are Tukey's outliers; lowercase letters indicate statistically different populations (Student's t-test, $p < 0.05$); red lines indicate linear regressions, with Pearson correlation coefficient R and corresponding p-value. (**h** to **k**) Schematic explanation of topology-derived turgor pressure heterogeneity. (h and i) Three-cell junctions in a tissue of hexagonal cells are at mechanical equilibrium with equal wall-wall angles. (j and k) Fewer-neighboured cells have sharper wall-wall angles, effectively resulting in mechanical compression due to unequal tension distribution (red dash-line arrow) that is balanced by higher turgor pressure build-up (big blue arrow).

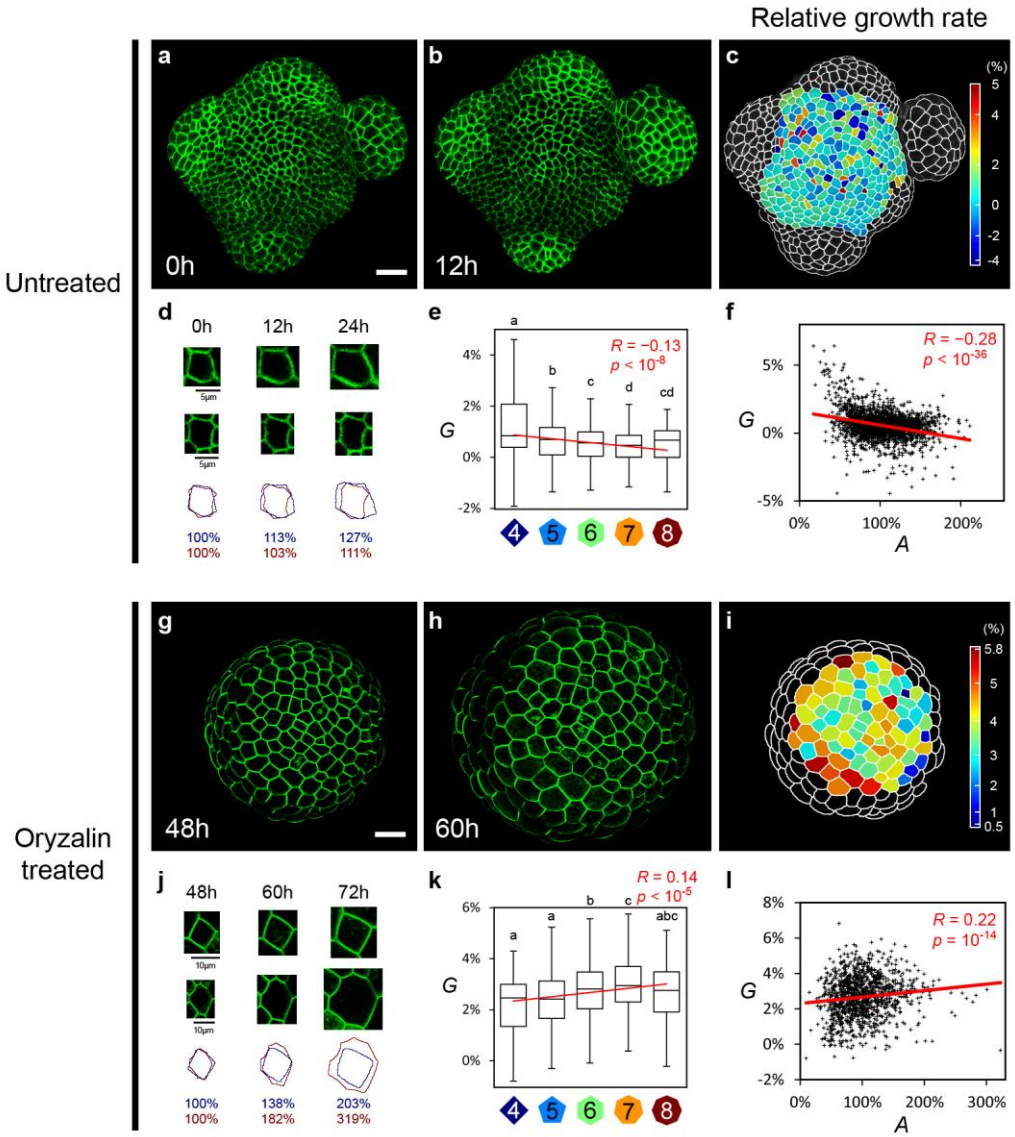

Figure 3. Cellular growth rate bifurcates between conditions.

(**a** to **f**) Relative growth rate per hour *G* of untreated SAM cells between 12-hour interval. (**g** to **l**) Cellular growth rate per hour of oryzalin-treated SAM between 12-hour interval (48 and 60 hours post treatment). (a, b, g and h) Surface projections of untreated or oryzalin-treated SAM at initial time point (a and g) and 12 hours later (b and h); scale bars are 20 μm unless otherwise noted. (c and i) Heat maps of areal relative growth rate per hour. Note that the colour lookup tables are exponential. (d and j) Example 4 and 8-neighbored cells during 24-hour growth, with areal normalization at initial time point. Cell contour and relative size (blue for 4-neighbored, red for 8-neighbored) depict the diverging growth trends. Scale bars are as indicated. (e, f, k and l) Box plots of relative growth rate per hour *G* against cell topology *N* (e and k) and dot plots of relative growth rate per hour *G* against normalized cell area *A* (f and l) (e and f, untreated 11 SAMs, $n = 2013$ cells; k and l, oryzalin-treated 14 SAMs, $n = 1160$ cells). Note that Tukey's outliers are not plotted, but are included for statistical analyses. Lowercase letters indicate statistically different populations (Student's *t*-test, $p < 0.05$); red lines indicate linear regressions, with Pearson correlation coefficient *R* and corresponding *p*-value.

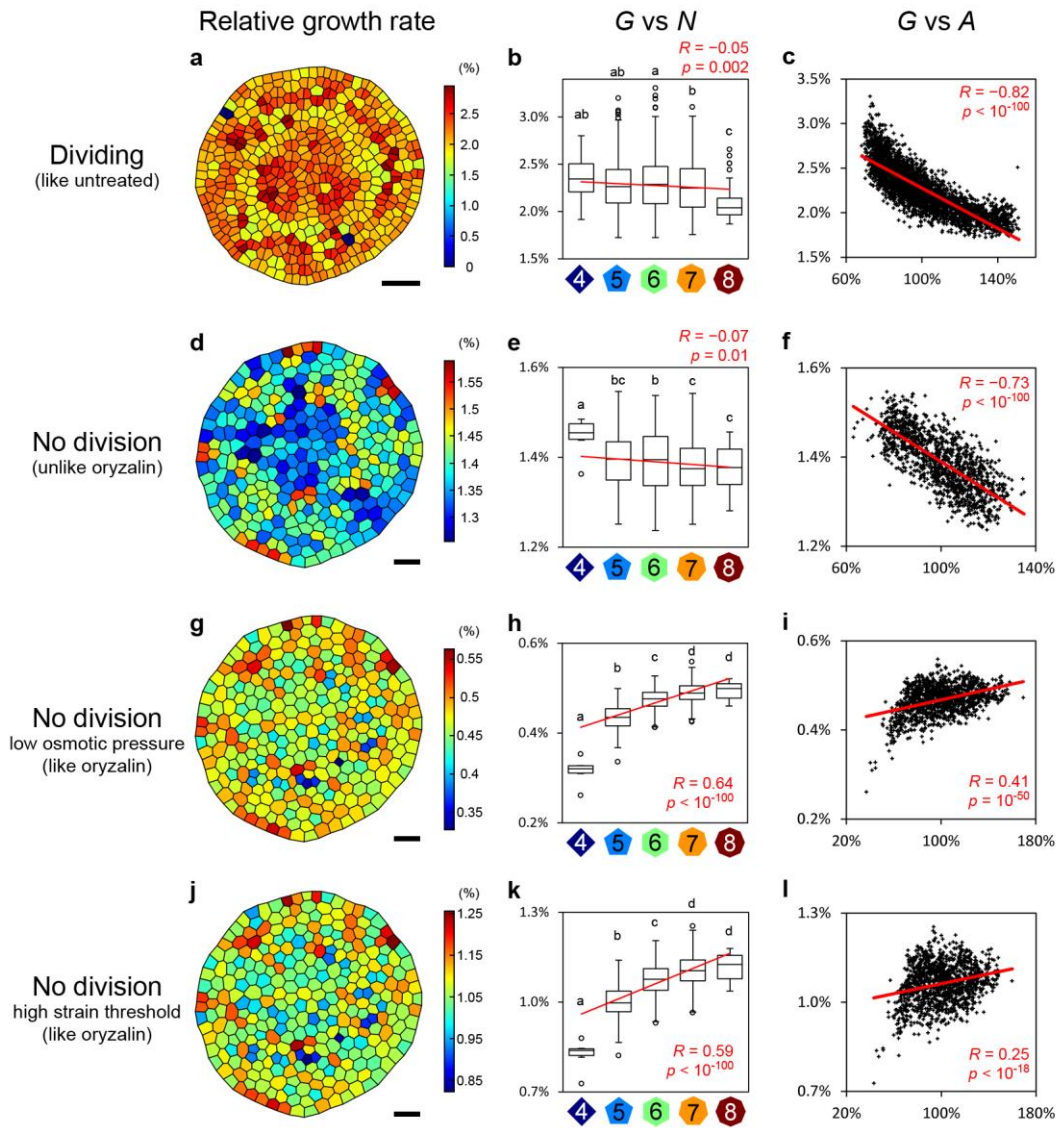

Figure 4. Reducing osmotic pressure or increasing growth threshold invert growth trend.

(**a** to **c**) Relative growth rate per hour *G* in simulations with cell division, which mimics untreated SAM. Cells that just divided (dark blue) are not included in analysis. (**d** to **f**) Growth simulations with no cell division to mimic oryzalin treatment. Growth does not recapitulate oryzalin-treated SAM. (**g** to **i**) Growth simulations with no division plus reduced osmotic pressure. Growth recapitulates oryzalin-treated SAM. (**j** to **l**) Growth simulations with no division plus elevated cell wall strain threshold. Growth also recapitulates oryzalin treatment. (a, d, g and j) Heat maps of areal relative growth rate per hour. Scale bars are 5 unit lengths. (b, e, h and k) Box plots of relative growth rate per hour *G* against cell topology *N* (b, dividing 8 simulations, $n = 3240$ cells; e, h and k, non-dividing 5 simulations each, $n = 1219$ cells). Lowercase letters indicate statistically different populations (Student's *t*-test, $p < 0.05$); red lines indicate linear regressions, with Pearson correlation coefficient *R* and corresponding *p*-value. (c, f, i and l) Dot plots of relative growth rate per hour *G* against normalized cell area *A*.

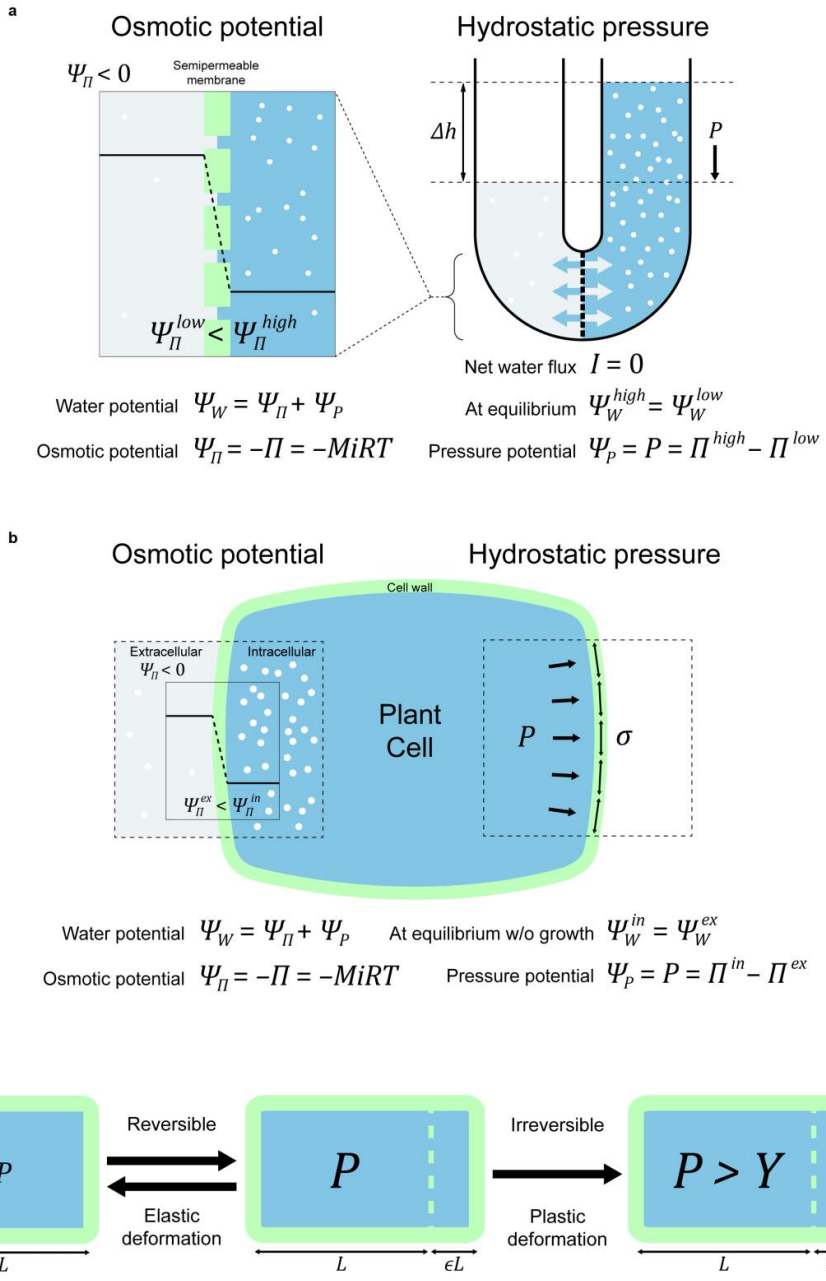

Extended Data Figure 1. Osmotic pressure, hydrostatic pressure and the Lockhart-Ortega equation of growth.

(**a**) Osmosis occurs when solutions of different osmotic pressure Π, due to different solute concentration (depicted by the density of white dots), are separated by a semipermeable membrane. Difference of osmotic potential Ψ_Π (depicted by horizontal black lines, always negative in solutions) across the membrane dictates that solvent flows from high to low potential compartment (low to high solute concentration). In a U-shaped tube setup (right), osmosis may stop before the two compartments reach the same concentration, as the extra volume (in fact height, Δh) in the higher-concentration compartment exerts a hydrostatic pressure P due to gravity that pushes the solvent back. P increases until reaching the same value as $\Delta\Pi$ at equilibrium where the total water potential Ψ_W is equal on both sides, and the net solvent flux $I = 0$ (indicated by the opposite blue arrows). M, solute molar concentration;

i, van t'Hoff index of solute that disassociates; *R*, ideal gas constant; *T*, absolute temperature. (**b**) Osmosis in a plant cell, where gravity is neglected for its small size. Because of the rigid cell wall that restricts the cell volume, hydrostatic pressure *P*, alias turgor pressure, builds up alongside cell wall tension σ to counterbalance the difference of osmotic potential Ψ_Π, until $P = \Delta\Pi$. (**c**) A schematic representation of the Lockhart-Ortega equation, where 1D cell length *L* elongation is a combination of reversible stretch ϵL (elasticity, ϵ is elastic strain) and cell wall yield ΔL at longer timescale (viscosity) if *P* is higher than a threshold *Y* (plasticity, $\Delta L = \varphi t L (P - Y)$, φ is wall extensibility, *t* is time).

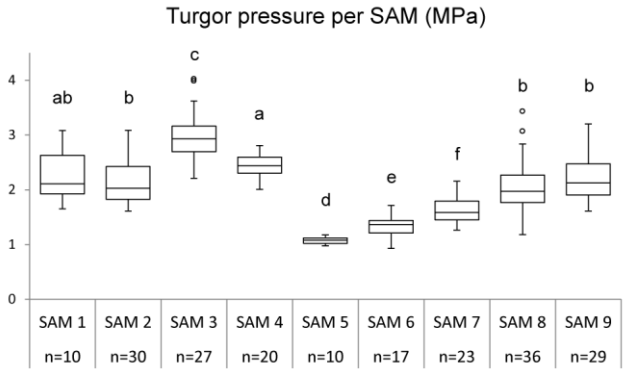

Extended Data Figure 2. Turgor pressure is highly heterogeneous between individual SAM.

All samples are oryzalin-treated SAM, *n* is cell number. Circles are Tukey's outliers; lowercase letters indicate statistically different populations (Student's *t*-test, $p < 0.05$).

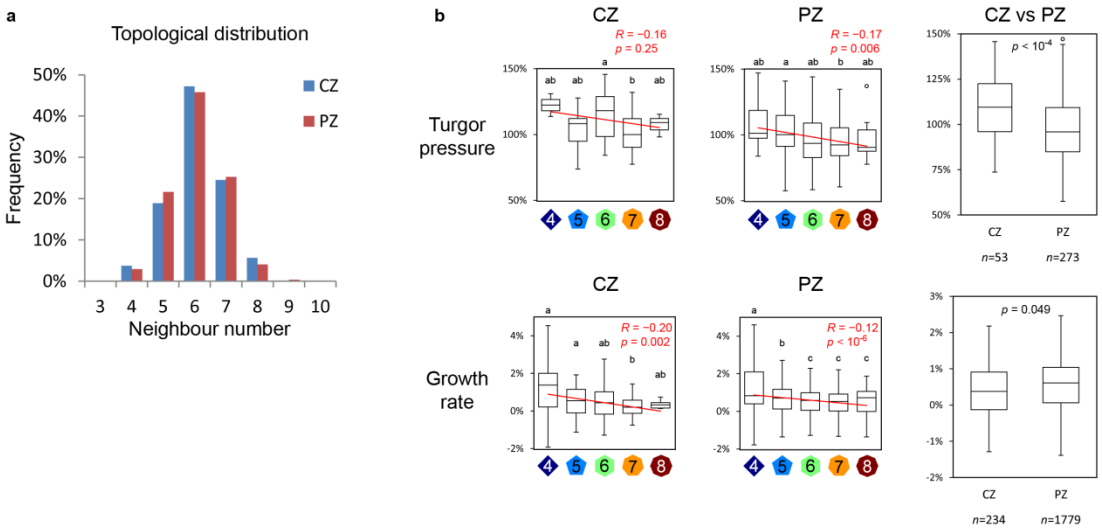

Extended Data Figure 3. Central zone and peripheral zone of untreated meristems have similar trends of turgor pressure and growth.

(**a**) Frequency of *N*-neighboured cells in central zone (CZ) and peripheral zone (PZ) shows no significant difference (Kolmogorov–Smirnov test, confidence level $\alpha = 0.05$, $D_{n,m} < D_{\alpha}$). (**b**) Both turgor pressure (upper) and growth rate per hour (lower) anticorrelate with cell neighbour number in CZ and PZ. Circles in box plots are Tukey's outliers; lowercase letters indicate statistically different populations (Student's *t*-test, $p < 0.05$); red lines indicate linear regressions, with Pearson correlation coefficient R and corresponding *p*-value. Tuckey's outliers are not plotted for growth rate vs neighbour number plots, but are included for statistical analyses. Note that CZ has higher turgor pressure, and grows slightly slower than PZ.

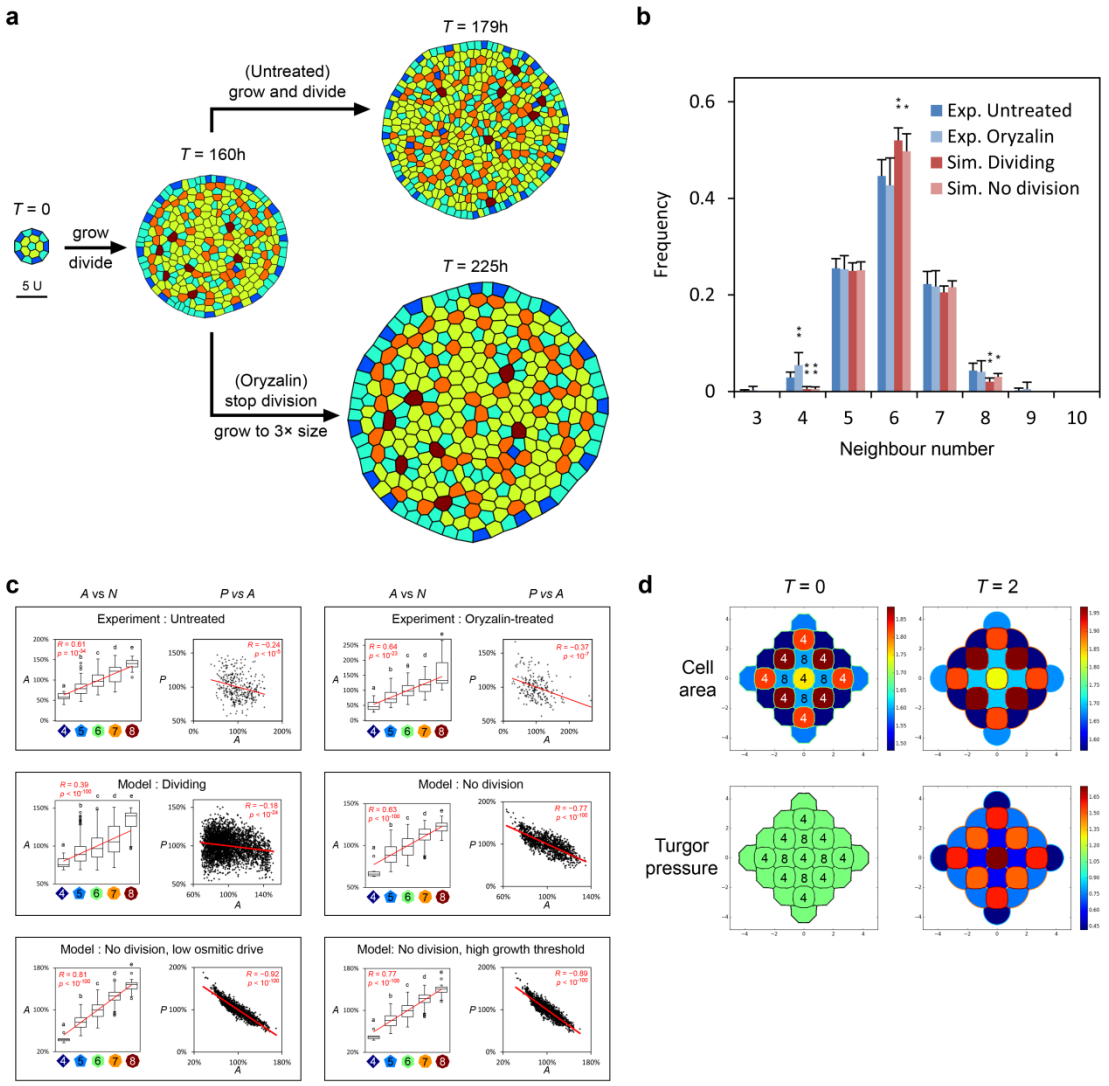

Extended Data Figure 4. Cell size and topology in SAM.

(**a**) Simulation checkpoints, where the initial mesh grows and divides until 160h, then division is stopped and parameters are changed to recapitulate oryzalin treatment, until the mesh reach a final size of 3 times of initial size. Scale is 5 unit length, colours indicate neighbour number. (**b**) Observed (Exp.) and simulated (Sim.) SAMs have similar topological distribution between different conditions, error bars are standard deviations. (**c**) Box plots of normalized cell area A against cell neighbour number N, and dot plots of normalized turgor pressure P against A in different experimental and simulation conditions, same data from Figure 1 to 4. Circles are Tukey's outliers; lowercase letters indicate statistically different populations (Student's t-test, $p < 0.05$); red lines indicate linear regressions, with Pearson correlation coefficient R and corresponding p-value. (**d**) Simulation with uncoupled cell size and topology (4-neighbored cells have bigger area than 8-neighbored cells) shows that turgor pressure builds up higher in fewer-neighboured cells, not smaller cells. This consolidates the topology-pressure correlation.

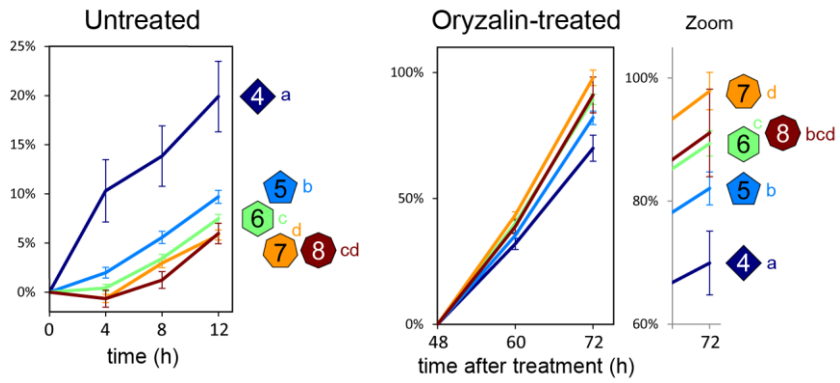

Extended Data Figure 5. Relative cell size increments confirm growth trend inversion between conditions.

Cell-specific relative areal increment $dA / A = A_t / A_0 - 1$ per topological category, computed from experimental observations. Line colours are topological categories indicated by the polygons, which are ranked high-to-low (top-to-bottom) next to the plots. Error bars are standard errors of means; lowercase letters indicate statistically different populations (Student's *t*-test, $p < 0.05$). The ranks show that fewer-neighboured cells grow more in untreated SAM (11 SAMs, $n = 2013$ cells) but grow less in oryzalin-treated SAM (14 SAMs, $n = 1160$ cells).

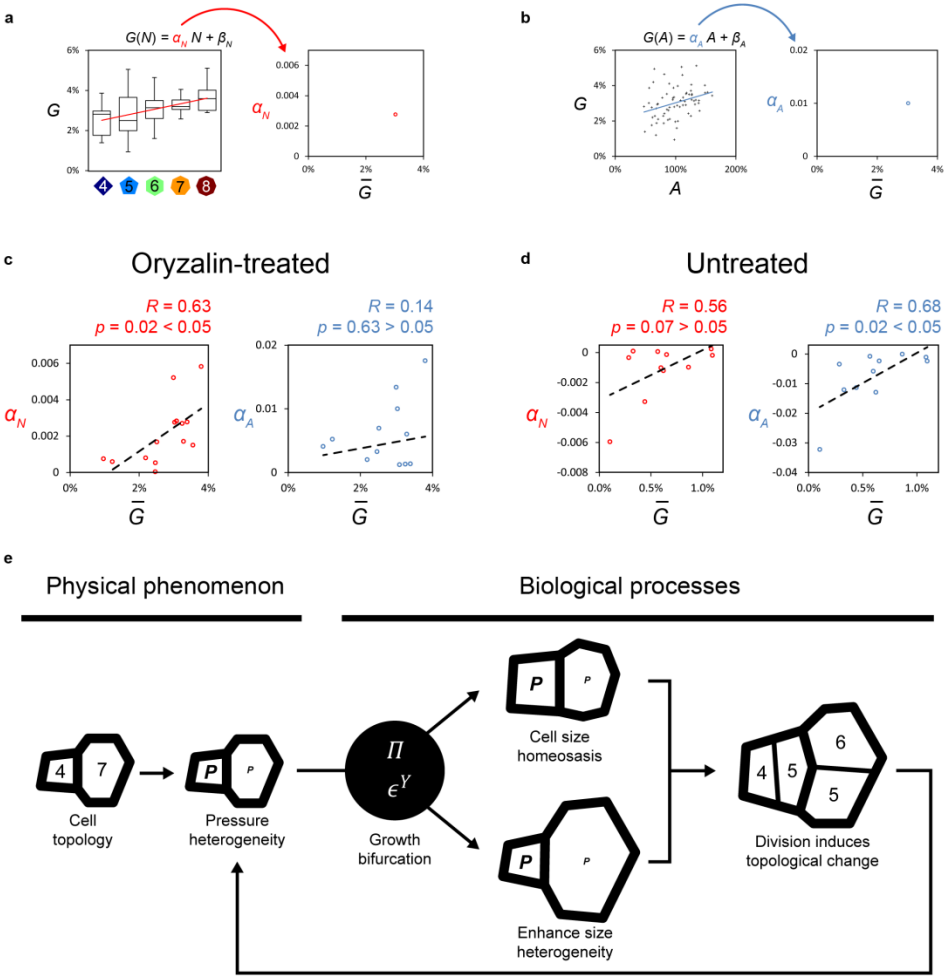

Extended Data Figure 6. Growth heterogeneity correlates with topology in oryzalin-treated SAM, but correlates with cell size in untreated SAM.

(**a** and **b**) Examples of cellular growth rate heterogeneity, depicted by the linear regression slope of growth rate G against topology N (α_N, red) or G against normalized cell area A (α_A, blue), plotted against average growth rate $\bar{G}$ of one individual oryzalin-treated SAM. β is regression intercept, which is not used here. (**c**) Among oryzalin-treated SAMs (n = 14), faster growing SAMs have bigger cellular growth heterogeneity against topology (bigger α_N), while growth heterogeneity against cell size α_A shows no significant correlation. (**d**) Untreated SAMs (n = 11) show significantly weaker growth heterogeneity against cell size in faster growing SAMs (note that most α_A are negative, depicting anticorrelation, so bigger α_A means slope closer to 0, thus smaller heterogeneity), while growth heterogeneity against topology α_N is less associated with SAM growth rate. Dotted black lines are linear regressions of α against $\bar{G}$, with Pearson correlation coefficient R and the corresponding p-value. (**e**) Schematic summary of heterogeneity in turgor pressure and growth rate. Heterogeneous turgor pressure emerges from tissue topology as a pure physical phenomenon, while growth rate bifurcates according to the controlling regimes that can be shifted biologically. Cell division causes topological changes that re-establish turgor pressure heterogeneity. P, turgor pressure; Π, osmotic pressure; ϵ^Y, strain threshold.

181

Methods

Plant materials, treatments and growth conditions

Arabidopsis thaliana GFP-LTi6b (ecotype WS-4) reporter line was used[31]. Untreated inflorescence meristems were obtained from soil-grown plants, first in short-day (8 h light 20 ℃ / 16 h dark 19 ℃ cycle) for 3 to 4 weeks then transferred to long-day (16 h light 20 ℃ / 8 h dark 19 ℃ cycle) for 1 to 2 weeks to synchronize bolting. Oryzalin-treated inflorescence meristems were obtained from plants grown on custom-made Arabidopsis medium[32] (Duchefa) supplemented with 1% agar-agar (Merck) and 10 µM N-1-naphthylphthalamic acid (NPA, Sigma-Aldrich/Merck) for 3 weeks. Pin-formed inflorescence meristems from NPA medium were immersed in 10 µg/mL oryzalin (Sigma-Aldrich/Merck) twice (3 h duration, 24 h interval)[19]. For mechanical measurements and time-lapse confocal imaging, meristems were mounted on Arabidopsis apex culture medium (ACM)[32] with 2% agarose and 0.1% plant preservation mixture (PPM, Plant Cell Technology) to prevent contamination, and cultivated in long-day condition.

Atomic force microscopy

Untreated meristems (dissected, with most late stage-2 floral primordia removed to prevent blocking of the cantilever) and oryzalin-treated meristems were mounted on ACM (2% agarose, 0.1% PPM) the night before. Drops of 2% low melting agarose (Duchefa) were applied around the lower parts of meristems for mechanical stabilization. For oryzalin-treated meristems, 72 h post-treatment meristems were measured.

AFM indentations were performed as in Beauzamy et al., 2015 [18]. Specifically, a BioScope Catalyst model AFM (Bruker) under a MacroFluo optical epifluorescence macroscope (Leica) was used. All measurements were done with customized 0.8 µm diameter spherical probes mounted on silicon cantilevers of 42 N/m spring constant (SD-Sphere-NCH-S-10, Nanosensors). Cantilever deflection sensitivity was calibrated against a clean sapphire wafer submerged in water before each session.

208 Meristems were submerged in water during AFM measurements. PeakForce QNM mode was
209 used to record sample surface topography and cell contours (aided by the stiffness difference
210 between periclinal and anticlinal cell walls on DMT modulus maps) in overlapping square
211 tiles of 30×30 to 50×50 μm^2 (128×128 pixels). Force curves were obtained by the
212 point-and-shoot mode of the Bruker software, with at least 3 locations chosen near the
213 barycentre of each cell, and 3 consecutive indentations per location, making at least 9 force
214 curves per cell. Approximately 10 μN maximum force was applied during each indentation,
215 corresponding to approximately 1 μm indentation depth.

216 **Force curve analysis**

217 Turgor pressure was determined as previously reported[18]. Specifically, cell wall elastic
218 modulus (Hertzian model, 1~10% maximal indentation force) and cell apparent stiffness
219 (linear, 75~99% maximal indentation force) were retrieved from each force curve by the
220 NanoScope Analysis software (Bruker). Quality of force curves were checked empirically and
221 by the fit coefficient of determination $r^2 > 0.99$. Cells with only low quality force curves were
222 not analysed. Cell surface curvatures (mean and Gaussian) were estimated from AFM
223 topographic images, with the curvature radii fitted to the long and short axes of each cell.
224 Turgor pressure was further deduced from each force curve (100 iterations) with the
225 simplified hypothesis that the surface periclinal cell walls has constant thickness (200 nm),
226 and cell-specific turgor pressure is retrieved by averaging all turgor deductions per cell.

227 For cell registration, confocal stacks of each meristem were obtained prior to AFM
228 measurements by an LSM 700 confocal (Carl Zeiss). Surface projection of *GFP-LTi6b* signal
229 was generated by the software MerryProj[33], then rescaled and rotated (affine transformation)
230 to overlay the AFM image tiles. The resulting surface projection image was used to generate
231 cell contour image of the whole meristemic surface using morphological segmentation
232 plugin[34] for the software ImageJ (https://fiji.sc/), while the relative positions of each AFM
233 indentation location is then registered onto the cell contour image, along with cellular
234 geometrical and topological analyses, using the NanoIndentation plugin for ImageJ[35].

235 Since each meristem had different turgor pressure range[20], cellular turgor pressure was

236 normalized to the average of each meristem for comparing cell-to-cell turgor pressure
237 heterogeneity without meristem-specific effects.

238 **Time-lapse confocal microscopy**

239 Untreated (dissected) and oryzalin-treated meristems were mounted and grown on ACM with
240 0.8% agarose and 0.1% PPM for live imaging. Confocal stacks were taken on an LSM 700
241 confocal with a W N-Achroplan 40x/0.75 M27 water immersion objective (Carl Zeiss) and a
242 TCS SP8 confocal (Leica) with a Fluotar VISIR 25x/0.95 water immersion lens. GFP was
243 excited at 488 nm and emission detected between 415 – 735 nm. Stacks have resolution of
244 1028×1028 pixels, with resolution ranging between 3.2 to 4.4 pixels/μm; Z steps were
245 between 0.5 and 0.85μm.

246 **Image processing and geometric analysis**

247 3D shell mesh and surface projection of untreated meristems were generated from confocal
248 stacks using the level set method (LSM) addon[36] for the software MorphoGraphX (MGX)[37].
249 For oryzalin-treated meristems, 2D surface projections were generated by MerryProj[33] and
250 imported into MGX for further processing. Projected images were segmented using watershed
251 method after manual seeding, and cell lineage between time points was manually assigned in
252 the meristem proper. A custom-made Python script was used to trace cell lineage between
253 multiple time points and determine cell topology based on the anticlinal wall number exported
254 from MGX. Areal relative exponential growth rate per hour was calculated as:

$$G = \frac{\ln(A_t/A_0)}{\Delta t}$$

255 where Δt is time interval in hours, A_0 is original cellular area at time t_0, and A_t is final area at
256 time $t_0 + \Delta t$. Cells undergone topological changes (i.e. divided cells and cells adjacent to new
257 division planes) during the acquisition were not included in the growth analyses.

258 For figure panels, brightness and contract of confocal images were linearly enhanced for
259 better visual. To synchronize panel shape and size, black background with no relevant
260 information was cropped from or added to the edge of the panels.

Statistical analysis

All Tukey box plots depict the first, second (median) and third quartiles of data distribution, with whiskers marking the lowest/highest data within 1.5 interquartile ranges (IQR) of the lower/upper quartiles. Tukey's outliers are depicted as small circles outside the whiskers. Absolute values like turgor pressure and cell area were normalized to the average per meristem, while relative values like growth rate do not require normalization. After normalization, every cell was consider as one biological sample, and all linear regressions and Pearson correlations were performed on whole datasets. For simulations, cells on the edge of the mesh were not analysed due to border effect. Extremely rare polygon classes (i.e. triangle and nonagon) were not shown on the box plots but were included in linear regression and Pearson correlation tests.

Modelling

Summary. We build a vertex-based model of plant tissues at cellular level that couples osmosis-driven hydraulic fluxes between cells and from apoplast with a fixed water potential, and cell wall mechanics which resists and grows under tension. Turgor and growth rate heterogeneities emerge from this coupling and from the heterogeneities in cells sizes and topology (number of neighbours).

We consider a collection of N polygonal cells $i = 1, \ldots, N$ that form a mesh; this mesh evolves with the appearance of new cells because of cell division. The walls between cells are discretized into one or several segments. Given the topology, the mesh is fully characterized by the position of the vertices. The walls are given a height h and a width w.

Cell wall rheology. The cell walls are modelled as a visco-elasto-plastic material, which would be equivalent to the Ortega model[17] in the case of an elongating cell. Let σ_k be the stress of a wall segment k; the constitutive law writes $\sigma_k = E_k \varepsilon_k^e$ where E_k is the elastic modulus and ε_k^e is the elastic deformation of the wall. Let l_k be the length of segment k, the rate of change of ε_k^e is given by:

$$\frac{\mathrm{d}\varepsilon_k^e}{\mathrm{d}t} + \frac{2w}{h}\phi_k^w E_k \max\left(0, \varepsilon_k^e - \varepsilon_k^Y\right) = \frac{1}{l_k}\frac{\mathrm{d}l_k}{\mathrm{d}t}$$

where ϕ_k^w is the extensibility and ε_k^Y is the yield deformation of segment *k*. Equivalently, we could define a yield stress.

Mechanical equilibrium. Let P_i be the turgor pressure in each cell *i*. The tissue being at every moment in a quasi-static equilibrium, pressure forces on wall edges and elastic forces within walls balance exactly at each vertex *v*:

$$\frac{1}{2}\sum_{k\in f(v)} \Delta_k P A_k \boldsymbol{n}_k + \sum_{k\in f(v)} E_k \varepsilon_k^e a_k \boldsymbol{e}_{k,v} = 0$$

Where *f*(*v*) is the set of walls adjacent to junction *v*, and $\Delta_k P = P_{k_1} - P_{k_2}$ is the pressure jump across wall face *k*, with $k_1 < k_2$ as indices of the cells separated by face *k*, $A_k = hl_k$ is the area of the face *k* on which pressure is exerted, $\boldsymbol{n}_k$ is the normal vector to face *k*, oriented from cell k_1 to cell k_2, and $a_k = hw$ is the cross-section of the face, on which the elastic stress is exerted; finally, $\boldsymbol{e}_{k,v}$ is the unit vector in the direction of face *k*, oriented from junction *v* to the other end of face *k*. In the case of a single cylindrical cell for which growth is restricted to its principal direction, the model is equivalent to the Lockhart-Ortega model.

Fluxes. For each cell *i*, the apoplasmic pathway is represented as a flux U_i^a (in volume per time unit) from the apoplast of constant water potential Ψ^a through a perfectly semi-permeable membrane: $U_i^a = A_i L_i^a (P^M - P_i)$, where A_i is the area of each cell in contact with the apoplast, L_i^a is the corresponding water conductivity, $P^M = \pi_i + \Psi^a$ is assumed constant, and π_i is the osmotic pressure of cell *i*.

The symplasmic pathway corresponds to flows that occur through plasmodesmata, channels between cells that convey both water and solutes. The symplasmic flows thus only depend on turgor pressure difference. Let L_{ij} be the symplasmic water conductivity corresponding to the interface between two neighbour cells *i* and *j*, and A_{ij} their contact area, both assumed symmetric: $L_{ij} = L_{ji}$ and $A_{ij} = A_{ji}$. The symplasmic flux U_{ji}^s (in volume per time unit) from cell *j* to *i* is defined by:

$$U_{ji}^{s} = A_{ij} L_{ij}^{s} \left(P_j - P_i\right)$$

Finally, the total water flux for cell i is the sum of the apoplasmic flux U_i^a and the symplasmic fluxes U_{ji}^s with all its neighbors, so that its volume variation can be expressed as:

$$\frac{\mathrm{d}V_i}{\mathrm{d}t} = A_i L_i^a (P^M - P_i) + \sum_{j \in n(i)} A_{ij} L_{ij}^s \left(P_j - P_i\right)$$

where $n(i)$ is the set of neighbours of cell i.

Cell division. Cells divide when they reach a target volume V_0; this value is fixed and equal for all the cells. The axis of division is chosen as follows: it passes through the centre of mass of the cell and minimizes the sum of the perimeters of the two daughter cells. Because cell plate is synthesized from the centre of the dividing cell and connects to old walls at the end of cytokinesis, the young wall is initially not stretched and the corresponding new edge is given an elastic deformation $\varepsilon_k^e = 0$. In order to introduce some variability in the simulations, we added some noise on two division parameters: the axis of division is translated along its normal unit vector by a random distance following the uniform distribution unif(–0.05, 0.05); and the target volume for division is multiplied for each cell by a random number following the uniform distribution unif(1 – 0.025, 1 + 0.025).

Numerical resolution. In the Lockhart-Ortega model, the compatibility between wall elongation and cell volume increase is automatically enforced through the geometrical constraint of unidirectional growth that leads to equal relative growth rate of the cell and strain rate of the walls. In our multicellular model, this equality is no longer true. Instead, the lengths $l(X)$ of the edges and the volumes $V(X)$ of the cells are expressed as functions of the positions X of the vertices; then, given an initial position X of the vertices and elastic deformation ε^e of the edges, the equations of wall rheology, mechanical equilibrium, and water fluxes form a closed set of equations with respect to the unknowns X, P, and ε^e that allow to predict their evolution.

To give an idea of the mathematical complexity of the problem, one may consider the

following example: in a connected tissue, if one cell is stretched and forced to increase its volume, an equal volume of water has to enter the cell, either from the apoplastic compartment or the neighbour cells. In the latter case, pressure should drop in the neighbour cells, which should attract water from their own neighbours, and this could propagate to further cells depending on the geometry of the tissue and the parameters. Volume and therefore positions of the vertices could be also affected. Finally, one can see that the interaction between hydraulics and mechanics implies long range interactions where pressure plays a key role. We developed an original algorithm and implemented it in an in-house code, where at each time step, the mechanical equilibrium is resolved under constraints on the cell volume (from the water fluxes), and constraints on the cells edges (from the rheological law of the walls).

The computations were run on a computer with a 3.6GHz Intel Xeon E5 processor, 64 GB of RAM, and running Linux Debian Stretch. The typical computing time was one week for each computation.

Procedure for the computations. We first run in parallel 8 computations with cell division with parameters (see below) chosen so that the model mimics the behaviour of the untreated meristems regarding turgor and growth rate; these computations were run until $t = 179.1$h. To mimic the oryzalin treatment, the current states of the "untreated" computations at $t = 160$h (around 300 cells) are used as initial conditions for the oryzalin case: division is stopped, and we run 5 computations either with the same parameters, or with some parameters modified so that the behaviour of the oryzalin treated meristems is recovered (see below); the computations are run until the total volume has been multiplied by three from this initial state.

Parameterization of the model. A first requirement is to ensure that mean turgor (resp. mean relative growth rate) is of the order of few MPa (resp. a few % per hour) as in experiments. The Lockhart-Ortega model – which is at the basis of the multicellular mode we use – provides a simple way to predict these two quantities (see Cheddadi et al., unpublished): first the yield turgor P^Y(above which growth occurs, which can be evaluated from E, ϵ^Y, h, w)

sets a lower bound for turgor, and $P^M = \Psi + \pi$ sets an upper bound, where $\Psi = -2$ MPa is the water potential of the apoplastic compartment; then one can estimate the relative growth rate as a function of L^a, ϕ^w, P^M, P^Y. The Lockhart-Ortega model shows that L^a and ϕ^w play a symmetric role in the limitation of growth (as two electrical resistances in series), but in the present multicellular setup, the exploration of the parameters space showed that only a flux-limitation (relatively low value of L^a) allows to capture both the untreated and oryzalin cases. Similarly, we chose a relatively low value of the cell-cell conductivity L^s so that the turgor heterogeneities do not vanish. Then, as explained in the main text, we chose the parameters of the untreated case so that the mechanical negative contribution to growth (cells with less neighbours are disfavoured) is minimized: this could be obtained by setting the osmotic pressure value far from the yield turgor P^Y. Conversely, the shift to the oryzalin regime was obtained by either increasing ϵ^Y and therefore P^Y by a factor 2, or by decreasing the osmotic pressure from 17 MPa to 9 MPa. The values of the parameters used in the untreated case are recapitulated in the table below.

Parameter	**Value**	**Parameter**	**Value**
Unit length	10 µm	Apoplasmic conductivity L^a	1.7×10^{-12} m MPa^{-1} s^{-1}
Cell height h	10 µm		
Cell wall thickness w	0.5 µm	Symplasmic conductivity L^s	1.97×10^{-13} m MPa^{-1} s^{-1}
Elastic modulus E	2252 MPa		
Wall extensibility ϕ^w	5.6×10^{-6} MPa s^{-1}	Osmotic pressure π	17 MPa
Strain threshold ϵ^Y	0.05		

Supplementary table 1. Parameters used for the untreated model.

Data availability

All materials, scripts and datasets generated and analysed during the current study are available from the corresponding authors upon reasonable request.

379 **References**

380 1. Hong, L. *et al.* Heterogeneity and Robustness in Plant Morphogenesis: From Cells to
381 Organs. *Annu. Rev. Plant Biol.* **69,** 469–495 (2018).
382 2. Kamimoto, K. *et al.* Heterogeneity and stochastic growth regulation of biliary epithelial
383 cells dictate dynamic epithelial tissue remodeling. *eLife* **5,** (2016).
384 3. Ietswaart, R., Rosa, S., Wu, Z., Dean, C. & Howard, M. Cell-Size-Dependent Transcription
385 of FLC and Its Antisense Long Non-coding RNA COOLAIR Explain Cell-to-Cell Expression
386 Variation. *Cell Syst.* **4,** 622-635.e9 (2017).
387 4. Long, Y. *et al.* In vivo FRET-FLIM reveals cell-type-specific protein interactions in
388 Arabidopsis roots. *Nature* **548,** 97–102 (2017).
389 5. Chubb, J. R. Symmetry breaking in development and stochastic gene expression. *Wiley*
390 *Interdiscip. Rev. Dev. Biol.* **6,** e284 (2017).
391 6. Donati, G. & Watt, F. M. Stem Cell Heterogeneity and Plasticity in Epithelia. *Cell Stem Cell*
392 **16,** 465–476 (2015).
393 7. Gerdes, M. J. *et al.* Emerging Understanding of Multiscale Tumor Heterogeneity. *Front.*
394 *Oncol.* **4,** (2014).
395 8. Eldar, A. & Elowitz, M. B. Functional roles for noise in genetic circuits. *Nature* **467,** 167–
396 173 (2010).
397 9. Watanabe, K., Umeda, T., Niwa, K., Naguro, I. & Ichijo, H. A PP6-ASK3 Module
398 Coordinates the Bidirectional Cell Volume Regulation under Osmotic Stress. *Cell Rep.* **22,**
399 2809–2817 (2018).
400 10. Xie, K., Yang, Y. & Jiang, H. Controlling Cellular Volume via Mechanical and Physical

401 Properties of Substrate. *Biophys. J.* **114,** 675–687 (2018).

402 11. Guo, M. *et al.* Cell volume change through water efflux impacts cell stiffness and stem
403 cell fate. *Proc. Natl. Acad. Sci.* **114,** E8618–E8627 (2017).

404 12. Dumais, J. & Forterre, Y. "Vegetable Dynamicks": The Role of Water in Plant Movements.
405 *Annu. Rev. Fluid Mech.* **44,** 453–478 (2012).

406 13. Stewart, M. P. *et al.* Hydrostatic pressure and the actomyosin cortex drive mitotic cell
407 rounding. *Nature* **469,** 226–230 (2011).

408 14. Montel, F. *et al.* Stress clamp experiments on multicellular tumor spheroids. *Phys. Rev.*
409 *Lett.* **107,** 188102 (2011).

410 15. Rojas, E. R. & Huang, K. C. Regulation of microbial growth by turgor pressure. *Curr. Opin.*
411 *Microbiol.* **42,** 62–70 (2017).

412 16. Kroeger, J. H., Zerzour, R. & Geitmann, A. Regulator or driving force? The role of turgor
413 pressure in oscillatory plant cell growth. *PloS One* **6,** e18549 (2011).

414 17. Ortega, J. K. Augmented growth equation for cell wall expansion. *Plant Physiol.* **79,** 318–
415 320 (1985).

416 18. Beauzamy, L., Derr, J. & Boudaoud, A. Quantifying Hydrostatic Pressure in Plant Cells by
417 Using Indentation with an Atomic Force Microscope. *Biophys. J.* **108,** 2448–2456 (2015).

418 19. Corson, F. *et al.* Turning a plant tissue into a living cell froth through isotropic growth.
419 *Proc. Natl. Acad. Sci. U. S. A.* **106,** 8453–8458 (2009).

420 20. Beauzamy, L., Louveaux, M., Hamant, O. & Boudaoud, A. Mechanically, the Shoot Apical
421 Meristem of Arabidopsis Behaves like a Shell Inflated by a Pressure of About 1 MPa.
422 *Front. Plant Sci.* **6,** (2015).

423 21. Ishihara, S. *et al.* Comparative study of non-invasive force and stress inference methods
424 in tissue. *Eur. Phys. J. E Soft Matter* **36,** 9859 (2013).
425 22. Lucas, W. J., Ham, B.-K. & Kim, J.-Y. Plasmodesmata - bridging the gap between
426 neighboring plant cells. *Trends Cell Biol.* **19,** 495–503 (2009).
427 23. Kumar, N. M. & Gilula, N. B. The Gap Junction Communication Channel. *Cell* **84,** 381–388
428 (1996).
429 24. McLean, P. F. & Cooley, L. Protein Equilibration through Somatic Ring Canals in
430 Drosophila. *Science* **340,** (2013).
431 25. Weaire, D. L. & Hutzler, S. *The Physics of Foams*. (Clarendon Press, 2001).
432 26. Gibson, W. T. & Gibson, M. C. Chapter 4 Cell Topology, Geometry, and Morphogenesis in
433 Proliferating Epithelia. in *Current Topics in Developmental Biology* **89,** 87–114 (Academic
434 Press, 2009).
435 27. Péret, B. *et al.* Auxin regulates aquaporin function to facilitate lateral root emergence.
436 *Nat. Cell Biol.* **14,** 991–998 (2012).
437 28. Serrano-Mislata, A., Schiessl, K. & Sablowski, R. Active Control of Cell Size Generates
438 Spatial Detail during Plant Organogenesis. *Curr. Biol.* **25,** 2991–2996 (2015).
439 29. Willis, L. *et al.* Cell size and growth regulation in the Arabidopsis thaliana apical stem cell
440 niche. *Proc. Natl. Acad. Sci. U. S. A.* **113,** E8238–E8246 (2016).
441 30. Tsugawa, S. *et al.* Clones of cells switch from reduction to enhancement of size variability
442 in Arabidopsis sepals. *Development* **144,** 4398–4405 (2017).
443

Methods References

31. Cutler, S. R., Ehrhardt, D. W., Griffitts, J. S. & Somerville, C. R. Random GFP∶cDNA fusions enable visualization of subcellular structures in cells of Arabidopsis at a high frequency. *Proc. Natl. Acad. Sci.* **97,** 3718–3723 (2000).

32. Stanislas, T., Hamant, O. & Traas, J. Chapter 11 - In-vivo analysis of morphogenesis in plants. in *Methods in Cell Biology* (ed. Lecuit, T.) **139,** 203–223 (Academic Press, 2017).

33. Reuille, P. B. de, Bohn-Courseau, I., Godin, C. & Traas, J. A protocol to analyse cellular dynamics during plant development. *Plant J.* **44,** 1045–1053 (2005).

34. Legland, D., Arganda-Carreras, I. & Andrey, P. MorphoLibJ: integrated library and plugins for mathematical morphology with ImageJ. *Bioinformatics* **32,** 3532–3534 (2016).

35. Mirabet, V. *et al.* NanoIndentation, an ImageJ Plugin for the Quantification of Cell Mechanics. *Methods Mol. Biol.* (in press).

36. Kiss, A. *et al.* Segmentation of 3D images of plant tissues at multiple scales using the level set method. *Plant Methods* **13,** 114 (2017).

37. Reuille, P. B. de *et al.* MorphoGraphX: A platform for quantifying morphogenesis in 4D. *eLife* **4,** e05864 (2015).